



Efficient H₂ production and TN removal for urine disposal using a novel photoelectrocatalytic system of Co₃O₄/BiVO₄ - MoNiCuO_x/Cu

Changhui Zhou^a, Jinhua Li^{a,*}, Jiachen Wang^a, Chaoyue Xie^a, Yan Zhang^a, Lei Li^a,
Tingsheng Zhou^a, Jing Bai^{a,c}, Hong Zhu^b, Baoxue Zhou^{a,c,*}

^a School of Environmental Science and Engineering, Key Laboratory of Thin Film and Microfabrication Technology (Ministry of Education), Shanghai Jiao Tong University, Shanghai 200240, PR China

^b University of Michigan-Shanghai Jiao Tong University Joint Institute, Shanghai Jiao Tong University, Shanghai 200240, PR China

^c Shanghai Institute of Pollution Control and Ecological Security, Shanghai 200092, PR China

ARTICLE INFO

Keywords:

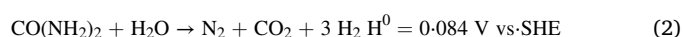
Urine treatment
Chlorine free radical
Hydrogen generation
Co₃O₄/BiVO₄ heterojunction
MoNiCuO_x/Cu cathode

ABSTRACT

Urea is considered as the potential hydrogen carrier. However, decomposition of urea to generate hydrogen gas (H₂) is severely constrained by sluggish kinetics and the high over-potential of HER. In this study, we propose a novel photoelectrocatalytic (PEC) system of Co₃O₄/BiVO₄ - MoNiCuO_x/Cu to realize efficiently H₂ production and TN removal in urine treatment. The key design is that an appropriate valence band position of BiVO₄ photoanode, which can generate Cl• selectively and suppress HO• extremely, is selected for rapidly converting urea to N₂ instead of NO₃. Co₃O₄, as a co-catalyst of photoanode, matches exactly the Fermi level with BiVO₄, driving the separation and transfer of photogenerated charge of BiVO₄ greatly due to the built-in electric field of p-n heterojunction of Co₃O₄/BiVO₄. Meanwhile, the yield of Cl• by Co₃O₄/BiVO₄ has been improved by an orders of magnitude compared with BiVO₄, WO₃ and TiO₂. On the other hand, the over-potential of HER is reduced to 49 mV (−10 mA cm^{−2}) by using MoNiCuO_x nanowires cathode, which is prepared by in-situ growth of nanowires and the load of MoNi sites on copper foam. The PEC system exhibits excellent performance, in which the H₂ production and TN removal were reached 0.68 mmol and 93.6% after 120 min, which is 2.4, 3.5, 11.0 times and 3.1, 4.6, 17.9 times respectively higher than those of BiVO₄, WO₃ and TiO₂. Therefore, this study provides new insights in urine treatment and H₂ generation.

1. Introduction

Urea (CO(NH₂)₂) is widely present in municipal domestic sewage and enriches 80% of nitrogen, in which discharge without effective treatment will cause eutrophication of water bodies [1–3]. Hence, different techniques are developed in the disposal of urine, such as biological technologies, electrochemical means and photochemical methods [1,4,5]. However, urea is the possible source of hydrogen, in which the recovery of hydrogen energy is often omitted [6]. Moreover, compared to water splitting (Eq. 1), H₂ production from urea decomposition has a relatively smaller potential (Eq. 2) [6,7].



Therefore, designing a novel urine treatment system to realize the rapid removal of total nitrogen (TN) and recovery of hydrogen energy is promising. However, the denitrification of urea undergoes the sluggish kinetics because of the occurrence on the surface of catalyst and the peroxidation of nitrate (NO₃). Interestingly, existing reports and our studies confirm that chlorine free radical (Cl•) is capable of rapidly converting nitrogen-compounds to N₂ instead of NO₃ due to its high activity and selectivity [5,8–12]. Hence, a technology for in-situ activation of Cl[−] to generate Cl• is designed, which can rationally utilize Cl[−] in urine and solve the problem of selective oxidation of urea to N₂ and inhibits the production of NO₃. Based on this design concept, how to further efficiently generate Cl• is the essential for urea degradation. Recently, photoelectrocatalysis (PEC) has attracted much attention, which can efficiently generate radicals [1,11,13,14]. Meanwhile, the

* Corresponding author at: School of Environmental Science and Engineering, Key Laboratory of Thin Film and Microfabrication Technology (Ministry of Education), Shanghai Jiao Tong University, Shanghai 200240, PR China.

** Corresponding author.

E-mail addresses: lijinhua@sjtu.edu.cn (J. Li), zhoubaoxue@sjtu.edu.cn (B. Zhou).

<https://doi.org/10.1016/j.apcatb.2022.122229>

Received 21 June 2022; Received in revised form 28 October 2022; Accepted 26 November 2022

Available online 29 November 2022

0926-3373/© 2022 Elsevier B.V. All rights reserved.

common photoanodes, such as WO_3 and TiO_2 [15–17], have been utilized in PEC systems, but the selectivity towards $\text{Cl}\bullet$ is relatively lower due to its un-match valence band position [18–22], which is easy to generate hydroxyl radical ($\text{HO}\bullet$) per-oxidizing urea to NO_3^- [23]. Undoubtedly, BiVO_4 (narrow band: 2.48 eV) is an alternative visible-light active photoanode due to its appropriate band gap, which can selectively generate $\text{Cl}\bullet$ and extremely suppress the generation of $\text{HO}\bullet$ [12, 14,24–26]. Besides, Co_3O_4 (narrow band: 1.81 eV) is another suitable catalyst in valence band position, in which the Fermi level exactly matches BiVO_4 and forms the p-n heterojunction [27–30]. Thereafter, the built-in electric field is formed in the $\text{Co}_3\text{O}_4/\text{BiVO}_4$ heterojunction, which drives electrons of Co_3O_4 into the conduction band (CB) of BiVO_4 , promotes the transfer of holes (h^+) of BiVO_4 to the valence band (VB) of Co_3O_4 , greatly reduces the recombination of photogenerated charges, and significantly improves the generation of $\text{Cl}\bullet$. Above, the constructed $\text{Co}_3\text{O}_4/\text{BiVO}_4$ photoanode can realize the efficient and highly selective generation of $\text{Cl}\bullet$, which overcome the slow degradation of urea and release hydrogen energy simultaneously.

On the other hand, the energy barrier (over-potential) of hydrogen evolution reaction (HER) on the cathode also needs to be resolved for efficient H_2 generation [31], in which the over-potential is prevalent in the reaction of hydrogen source decomposition [32]. Notably, platinum (Pt) has the lowest over-potential in the field of HER, but scarcity and high cost still hinder its further development [33]. Therefore, it is the reliable strategy to design the non-noble metal catalyst by referring to the reaction kinetics occurring on the Pt surface. Fortunately, some scholars have found that molybdenum nickel (MoNi) based catalysts have outstanding HER capabilities comparable to Pt [34–37]. Notably, how to expose fully the catalytically MoNi sites is important for HER, which will severely determine the H_2 generation [36]. Critically, our previous studies found that the three-dimensional (3D) porous structure of copper foam with good electrical conductivity, low resistance and large specific surface area is used as the substrate [38–40]. Besides, the construction of one-dimensional (1D) nanowires structures on the surface of copper foam supplies numerous catalytic support, which capable of supporting considerable MoNi catalytic active sites, thereby exposing sufficient catalytic active sites for to lower the energy barrier for HER [23,41,42]. Therefore, we designed a novel 3D catalyst consisting of arrays of highly exposed molybdenum nickel copper alloy oxide (MoNiCuO_x) nanowires on copper foam ($\text{MoNiCuO}_x/\text{Cu}$) to efficiently reduce the over-potential of HER, in which MoNiCuO_x nanowires are prepared by in-situ growth of $\text{Cu}(\text{OH})_2$ nanowires on copper foam and load of molybdenum nickel (MoNi) alloy sites on $\text{Cu}(\text{OH})_2$ nanowires. The results confirmed the over-potential to attain -10 mA cm^{-2} of $\text{MoNiCuO}_x/\text{Cu}$ cathode is 49 mV, which was lower than Pt (119 mV).

Thus, we propose a novel photoelectrocatalytic system combining $\text{Co}_3\text{O}_4/\text{BiVO}_4$ photoanode and $\text{MoNiCuO}_x/\text{Cu}$ cathode to realize H_2 production and TN removal simultaneously in the urine treatment. In the anode chamber, the h^+ of $\text{Co}_3\text{O}_4/\text{BiVO}_4$ heterojunction efficiently oxidize Cl^- to $\text{Cl}\bullet$ and further convert urea to N_2 and CO_2 with avoiding NO_3^- generation under irradiation of visible light, in which TN removal is 3.1 times, 4.6 times and 17.9 times higher than the BiVO_4 , WO_3 and TiO_2 , respectively. In the cathode chamber, the electrons generated during urea oxidation are transferred to the cathode through the external wire to reduce the H^+ on the surface of $\text{MoNiCuO}_x/\text{Cu}$ nanowires. Meanwhile, a large number of MoNi alloy sites with excellent hydrogen evolution properties are widely distributed in the $\text{MoNiCuO}_x/\text{Cu}$ cathode, which greatly reduces the over-potential of HER. Besides, H^+ passes through the proton exchange membrane (PEM) to equilibrate the concentration of H^+ in the dual chamber. Ultimately, an extremely efficient H_2 generation was obtained, in which it is 2.4 times, 3.5 times and 11.0 times and higher than the BiVO_4 , WO_3 and TiO_2 , respectively. The results show that the urea is rapidly decomposed and H_2 is effectively generated synchronously. This study offers a new insight for urine remediation and recovery of hydrogen energy.

2. Experiment section

2.1. Chemicals and materials

All of analytical reagent grade reagents were purchased from Sino-pharm Chemical Reagent Co., Ltd., China. Fluorine-doped tin oxide (FTO: $13 \Omega \text{ cm}^{-1}$) and copper foam (1 mm thick) were purchased from Nippon Sheet Glass and Suzhou Taili Metal Foam Co., Ltd., China, separately. Ultra-pure Deionized (DI) water was used to prepare the various required solutions. Meanwhile, the urea in simulated urine and actual urine were employed as the targets and diluted to 30 mg N L^{-1} , in which the simulated urine was prepared as initial urine sample described in Table S1 [11].

2.2. Preparation of electrodes

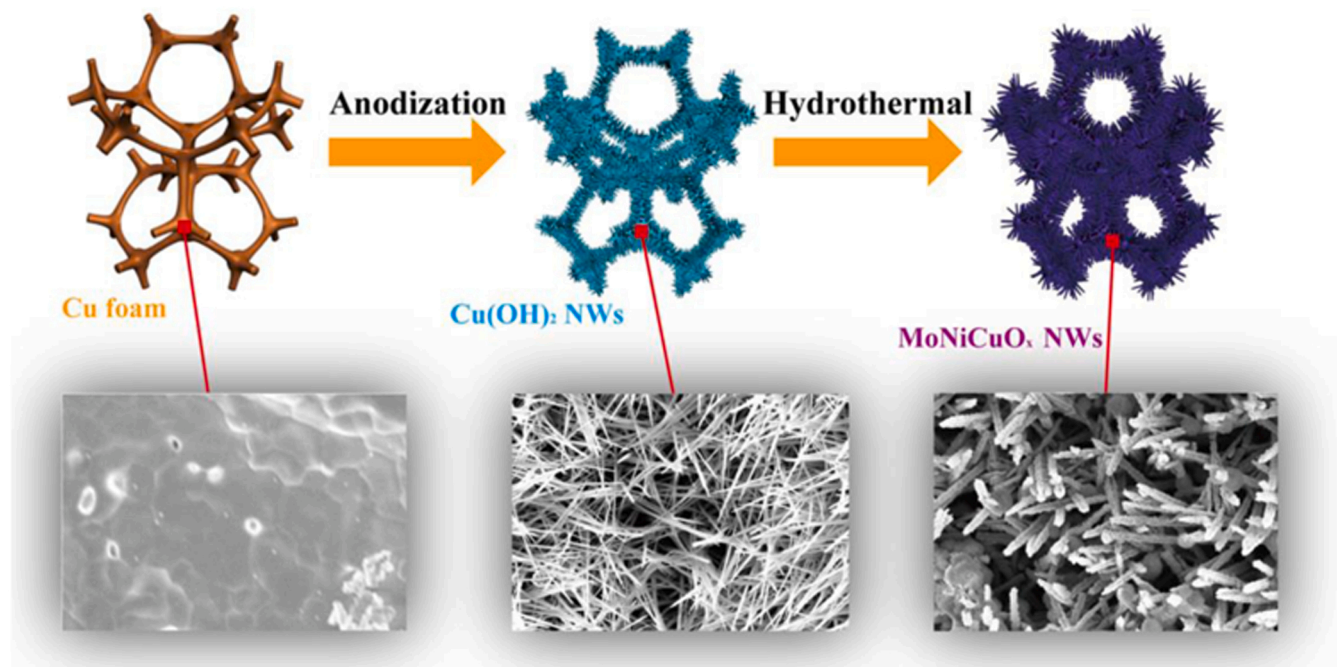
The $\text{MoNiCuO}_x/\text{Cu}$ cathode was synthesized by anodization and hydrothermal processes and the detailed was provided in Supplementary material [43,44]: firstly, the smooth copper foam was used anodization process to grow $\text{Cu}(\text{OH})_2$ nanowires, in which dense and slim $\text{Cu}(\text{OH})_2$ nanowires uniformly grown on the surface of the copper foam. Then treated copper foam was consequently treated hydrothermally. Finally, the obtained black $\text{MoNiCuO}_x/\text{Cu}$ was vacuum dried overnight, in which $\text{Cu}(\text{OH})_2$ nanowires became rough and uniformly covered with MoNiO_x alloy (Scheme 1). Additionally, the preparation details of $\text{Co}_3\text{O}_4/\text{BiVO}_4$ nanorods are shown in the Supplementary material according to previous works [27,28].

2.3. Experimental setup

The double chamber reactor, assembled from quartz glasses, was equipped for denitrification and hydrogen production (Fig. S1). Meanwhile, the cathode and anode chambers are separated by a proton exchange membrane (PEM), on which H^+ in the anode chamber entered into the cathode chamber through PEM. Moreover, $\text{Co}_3\text{O}_4/\text{BiVO}_4$, as the working electrode, was placed in the anode chamber facing the light source; Ag/AgCl , as the reference electrode, was also placed in the anode chamber; $\text{MoNiCuO}_x/\text{Cu}$, as the counter electrode, was placed in the cathode chamber parallel to the working electrode. The simulated urine (100 mL), 50 mM Na_2SO_4 and 50 mM NaCl were placed in the anode chamber, and the cathode chamber added 50 mM Na_2SO_4 as the electrolyte. Additionally, a 350 W xenon lamp (Perfect, China) provided a light intensity of 100 mW cm^{-2} as a simulated solar light source.

2.4. Analytical methods

A scanning electron microscope (SEM, Zeiss SUPRA55-VP), X-ray diffractometer (XRD, Rigaku D-Max B), X-ray photo-electron spectroscopy, Ultraviolet photoelectron spectroscopy (XPS, UPS, AXIS UltraDLD) and high-resolution transmission electron microscope (HRTEM) coupled with an X-ray energy dispersive spectrometer (EDS) were used to characterize the different properties of the prepared electrodes, respectively. Besides, the colorimetric method applying with a UV-visible spectrophotometer (752 N, INESA, Shanghai) was used to determine the concentration of active chlorine, nitrate and ammonia. Additionally, TN/TOC analyzer (Analytikjena, Germany) was used to detect TN and TOC. The electron spin resonance method (ESR, Micro ESR, USA) was to detect the free radical species. The high performance liquid chromatography (HPLC-2010 Plus, Shimadzu) was applied to determine the concentration of urea. The generated gases (N_2 and H_2) were analyzed by on-line GC (Fuli Instruments, 9790Plus, China). Moreover, the detailed and data-processing methods was provided in the Supplementary material.



Scheme 1. Scheme illustration of the fabrication procedures of the MoNiCuO_x/Cu electrode.

3. Results and discussions

3.1. Characterization of MoNiCuO_x/Cu cathode

The MoNiCuO_x/Cu was successfully prepared by two steps (Scheme 1). Fig. 1a and the high-magnification image (Fig. 1b) further showed the specific surface morphology, in which the surface of the MoNiCuO_x nanowires became much more rough. Besides, compared to smooth Cu(OH)₂ nanowires, MoNiCuO_x nanowires displayed no obvious change in length while became significantly thicker in diameter. In Fig. S3, the XRD patterns of the copper foam (Cu), Cu(OH)₂/Cu and MoNiCuO_x/Cu were displayed, in which the diffraction peaks at 43.3°, 50.4° and 74.1° originate from the Cu, and the peaks situated at 23.8°, 33.7° and 39.8° are confirmed to Cu(OH)₂ [45]. The peaks located at 30.1° and 41.7° are represented to MoNi₄, separately [46]. Besides, the peak situated at 24.5°, 35.7° and 61.0° are indicated MoO₂ [44]. Moreover, the peaks

located at 27.4° and 31.0°, which corresponded to the characteristic diffractions of CuO. These results indicated that MoNi₄ and MoO₂ were effectively covered on the surface of Cu(OH)₂ nanowires. Additionally, the high-resolution transmission electron microscopy (HRTEM) images of the MoNiCuO_x/Cu was shown in Fig. 1c-d, the lattice fringes with lattice spacing of 0.28 nm was corresponded to the (200) facet of MoNi₄ [44]. Moreover, lattice spacing of 0.35 nm was indicated to the (110) facet of MoO₂ [44]. The results further confirmed the MoNi₄ and MoO₂ were uniformly anchored on Cu(OH)₂ nanowires. Clearly, the TEM-EDX characterizations were signified the nanowire was composed of Cu, Mo, Ni and O elements.

Notably, the detailed chemical composition and element valance states of MoNiCuO_x/Cu were further provided by X-ray photoelectron spectroscopy (XPS) to further characterize. As shown in Fig. 2a, the prepared MoNiCuO_x/Cu electrode contained four elements of Mo, Ni, Cu and O, on which the corresponding characteristic peaks appeared in the

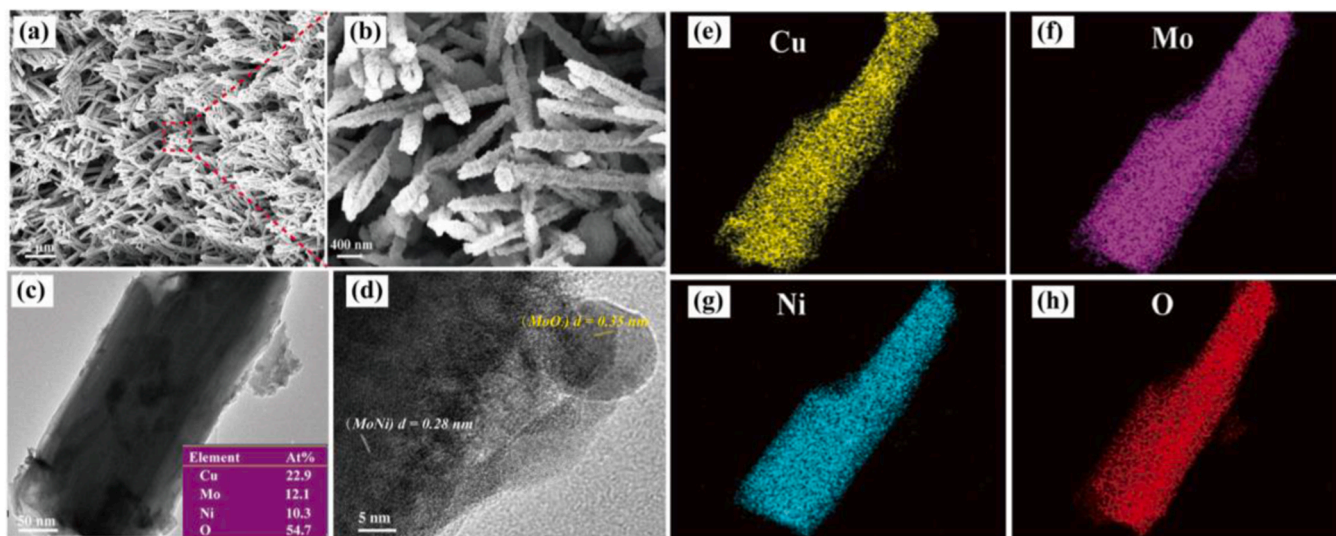


Fig. 1. (a) and (b) SEM images of MoNiCuO_x/Cu electrode; (c) TEM, (d) HRTEM images and (e-h) EDX mapping images of MoNiCuO_x/Cu electrode.

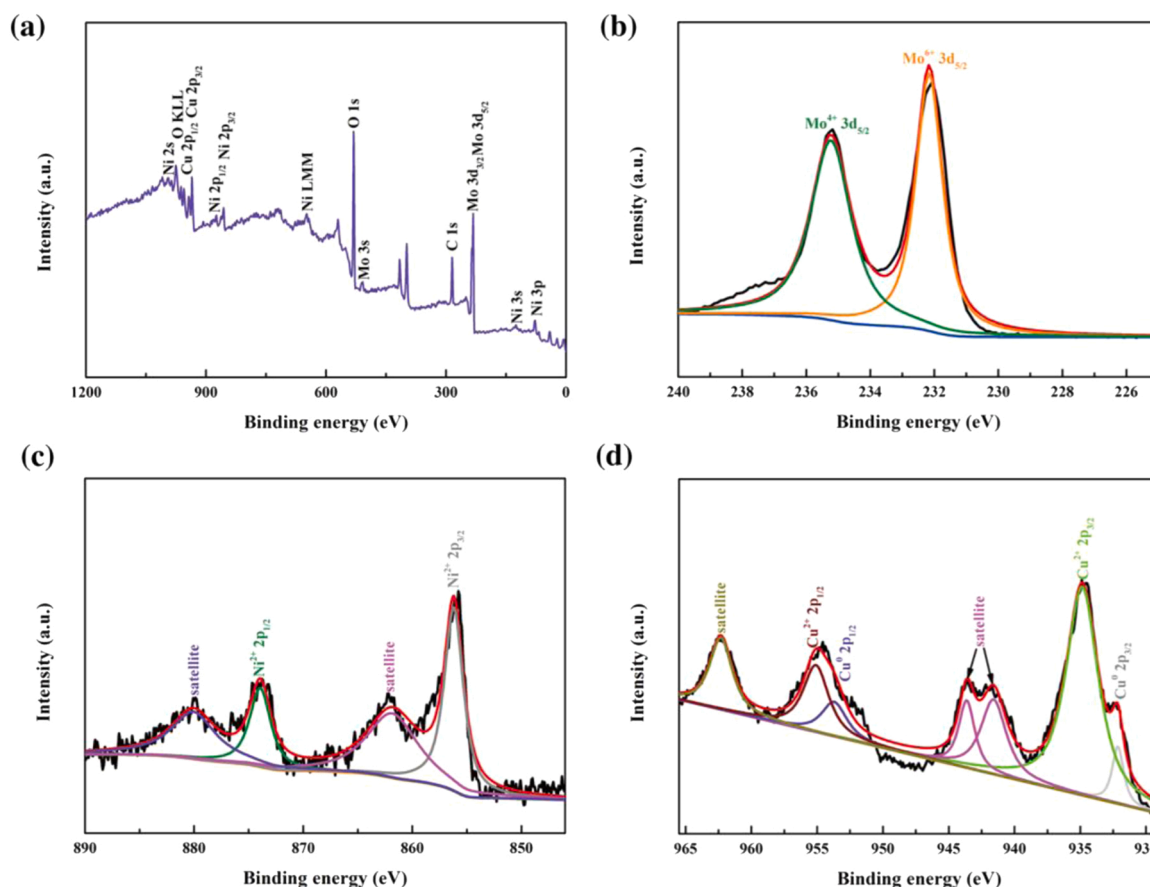


Fig. 2. (a) XPS patterns of (a) MoNiCuO_x/Cu electrode; (b) Mo 3d peak, (c) Ni 2p peak and (d) Cu 2p peak.

XPS spectrum. Besides, the high resolution spectrum of Mo 3d, Ni 2p and Cu 2p were shown in Fig. 2b-d, respectively. The Mo 3d spectrum can be divided into two high-intensity peaks, which at 235.2 eV (Mo⁴⁺) and 232.2 eV (Mo⁶⁺), separately [36]. In addition, the spectrum of Ni was divided into four peaks. Meanwhile, Ni²⁺ 2p_{3/2} and 2p_{1/2} showed the major two peaks with high intensity at 856.2 and 874.0 eV, while the other peaks were the satellites [36]. Additionally, the spectrum of Cu was divided into seven peaks, in which the two high-intensity peaks locating at 934.8 and 955.1 eV were indexed to Cu²⁺ 2p_{3/2} and 2p_{1/2}, while the two low-intensity peaks emerging at 932.1 and 953.6 eV were assigned to Cu⁰ 2p_{3/2} and 2p_{1/2} [45]. Similarly, the spectrum of Cu appeared the satellites.

After identifying the prepared MoNiCuO_x/Cu electrode, the hydrogen evolution reaction (HER) performances, as the most important property, was examined by different electrodes. Platinum (Pt) was the most outstanding HER material according to previous studies. Hence, we tested the linear sweep voltammetry (LSV) curves to compare the prepared cathode with Pt. Meanwhile, MoNiCuO_x/Cu cathode showed the most superior HER performance among all compared Pt and copper foam (Cu), exhibiting the lowest onset over-potential to attain -10 mA cm^{-2} . Significantly, the over-potential of MoNiCuO_x/Cu was 49 mV, which was much smaller than Cu (346 mV) and Pt (119 mV), respectively. Moreover, the HER performance of MoNiCuO_x/Cu was the most outstanding than listed in Fig. 3c, of which the specific details are displayed in the Table S2. Meanwhile, the over-potentials of both Cu (OH)₂/Cu (147 mV) and MoNiO_x/Cu (103 mV) were smaller than Cu, which confirmed the Cu(OH)₂ catalytic supports and MoNi catalytic sties both could reduce the over-potential of HER[39,44]. Besides, the Tafel slopes sourced from the LSV polarization curves was another key parameter to indicate the reaction kinetics of hydrogen evolution. As shown in Fig. 3b, the Tafel slope of MoNiCuO_x/Cu cathode was only

75 mV dec⁻¹ while the Tafel slope of Cu and Pt were 209 mV dec⁻¹ and 127 mV dec⁻¹, which further explaining the most optimal H₂O adsorption and hydrogen desorption processes. Besides, the Tafel slope was dropped from 209 mV dec⁻¹ to 75 mV dec⁻¹ after modified MoNiCuO_x nanowires, declaring the both Volmer step and Tafel step had been dramatically accelerated. Therefore, we proposed a possible process for the dissociation of H₂O molecules in MoNiCuO_x nanowires (Fig. S4), in which the hydrogen atom of H₂O molecules was adsorbed and activated on the MoNi₄ active sites. Then, the hydrogen atom was activated to form active hydrogen (H*), and H* was desorbed from MoNiCuO_x nanowires with the catalysis of MoO₂. Moreover, the density functional theory (DFT) calculations were applied to estimate the adsorption energies and the Gibbs free energy changes for H₂O adsorption ($\Delta G_{\text{H}_2\text{O}}$) and H₂ formation (ΔG_{H_2}), of which the structures and the calculated energies were displayed in Fig. S5. As shown in Fig. S5e, H₂O adsorption on the surface of MoNi₄ ($\Delta G_{\text{H}_2\text{O}} = -0.59 \text{ eV}$) was much more favorable than MoO₂ ($\Delta G_{\text{H}_2\text{O}} = -0.25 \text{ eV}$), but MoO₂ had a small energy barrier for the H₂ formation ($|\Delta G_{\text{H}_2}|$) (0.09 eV). Conversely, although MoNi₄ had a sluggish process in H₂ formation, the free energy values implied a more favorable H₂O adsorption on MoNi₄ active sites (Fig. S5f). Thus, the active sites of MoNi₄ and MoO₂ together promoted the HER, which further demonstrated the possible HER reaction on MoNiCuO_x nanowires. Besides, electrochemical surface area (ECSA) was calculated from cyclic voltammetry (CV) curves using the principle of electrochemical double layer capacitance, in which the ECSA was 4.9 times higher after modification of MoNiCuO_x nanowires (Fig. S6), indicating the large specific surface for HER performance. Actually, the excellent properties of ideal MoNiCuO_x/Cu electrode also need to include stability. Fig. 3d revealed the stabilized over-potential at the current density of -10 mA cm^{-2} , and there was no obvious variation in polarization curve between initial test and after multi-current

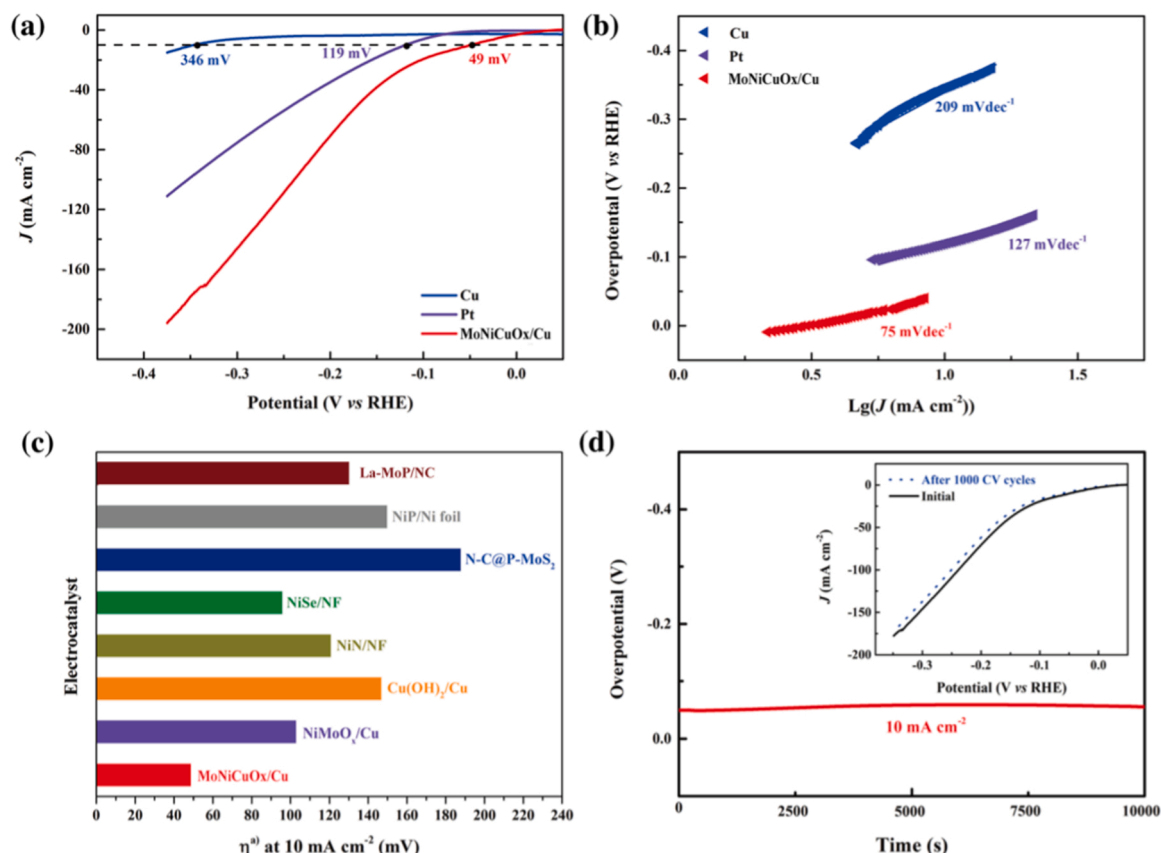


Fig. 3. (a) LSV curves of all compared electrodes tested at 1 M KOH with scanning rate of 10 mV s⁻¹; (b) Tafel slopes of contrastive electrodes; (c) Comparison of the current densities at -10 mV among different water alkaline electrodes; (d) Polarization curves of MoNiCuO_x/Cu electrode at the initial cycle and after 1000 cycles.

stability test, proving its superior durability.

3.2. Characterization of Co₃O₄/BiVO₄ photoanode

In order to confirm the success preparation of Co₃O₄/BiVO₄, FE-SEM was used to characterize the morphology of BiVO₄ and Co₃O₄/BiVO₄. In Fig. S7a-b, the appearance of Co₃O₄/BiVO₄ exhibited no obvious difference after the loading of Co₃O₄. However, it could be found that the surface of the nano-pillared BiVO₄ became rough and appeared some particles at higher magnification, which were the anchored Co₃O₄ [27]. Moreover, in the cross-sectional images (Fig. S8), the thickness of BiVO₄ film was 1.58 μm while the thickness of film was increased to 1.71 μm after the modification of Co₃O₄. Besides, the EDS results (Fig. S6c-f) further confirmed the Co element was modified on BiVO₄, which indirectly indicated the Co₃O₄.

Additionally, the XRD pattern was utilized to further characterize success preparation of Co₃O₄/BiVO₄. As shown in Fig. S8a, XRD patterns of BiVO₄ and Co₃O₄/BiVO₄ appeared the similar peaks located at 30.5°, 33.6°, 34.6°, 35.1° and 37.7°, which corresponded to the characteristic diffractions of BiVO₄ [28]. Moreover, there was a peak located at 37.3° on XRD pattern Co₃O₄/BiVO₄, which was characteristic peak of Co₃O₄ [47]. Besides, XPS spectra was applied to survey the chemical composition and valence state of Co₃O₄/BiVO₄ and the results were displayed in Fig. S8b-e. Meanwhile, four characteristic peaks corresponded to the elements of Bi, V, Co and O appeared in the XPS spectrum in Fig. S8b. The high resolution spectrum of Bi 4f, V 2p and Co 2p were shown in Fig. S8c-e, respectively. Specifically, the characteristic peaks which binding energies located at 797.3 and 781.3 eV can be assigned to the splitting orbital of Co 2p_{1/2} and Co 2p_{3/2}, and the other existence of peaks located at 803.6 and 785.7 eV were the satellites of Co [27]. Based on the above results, there was a strong proof of successful preparation of

Co₃O₄/BiVO₄.

To better characterize the performance of the Co₃O₄/BiVO₄ photoanode, LSV curves and electrochemical impedance spectroscopy (EIS) spectra were measured. As shown in Fig. 4a, the photocurrent density of WO₃ and TiO₂ (conventional semiconductors) are 1.31 and 0.08 mA cm⁻² at 1.36 V (vs. RHE), respectively. Correspondingly, the photocurrent density of BiVO₄ was 1.33 mA cm⁻² at 1.36 V (vs. RHE) while increased to 2.26 mA cm⁻² after fabricating the Co₃O₄/BiVO₄ p-n heterojunction, of which the built-in electric field (the space charge layer with opposite charge) can be formed on the interface between p-Co₃O₄ and n-BiVO₄. Moreover, the applied-bias photon-to-current metric (ABPC) of BiVO₄ and Co₃O₄/BiVO₄ were estimated (Fig. S10). Meanwhile, the value of Co₃O₄/BiVO₄ is 0.33%, which is almost 2 times of bare BiVO₄, further revealing that p-n heterojunction possesses stronger catalytic activity in the PEC system. The reason was that the built-in electric field can drive photogenerated electrons of p-Co₃O₄ into the conduction band (CB) of n-BiVO₄ and facilitate the valence band transfer of photogenerated holes (h⁺) in n-BiVO₄ to p-Co₃O₄, thereby greatly reducing the recombination of the photogenerated charges of BiVO₄ and Co₃O₄, and greatly increasing the photocurrent [29]. Besides, the EIS Nyquist analysis of BiVO₄ and Co₃O₄/BiVO₄ were conducted, in which the diameter of the fitted semicircle represents the charge transfer resistance, inversely to the rate of charge transfer the electrode. Meanwhile, the Nyquist plot of Co₃O₄/BiVO₄ was much narrower semicircle diameter than BiVO₄, which indicated the resistance of BiVO₄ was dramatically decreased after forming the Co₃O₄/BiVO₄ p-n heterojunction (Fig. 4b).

3.3. Urea removal and hydrogen generation

The improvement of Co₃O₄/BiVO₄ for denitrification and H₂

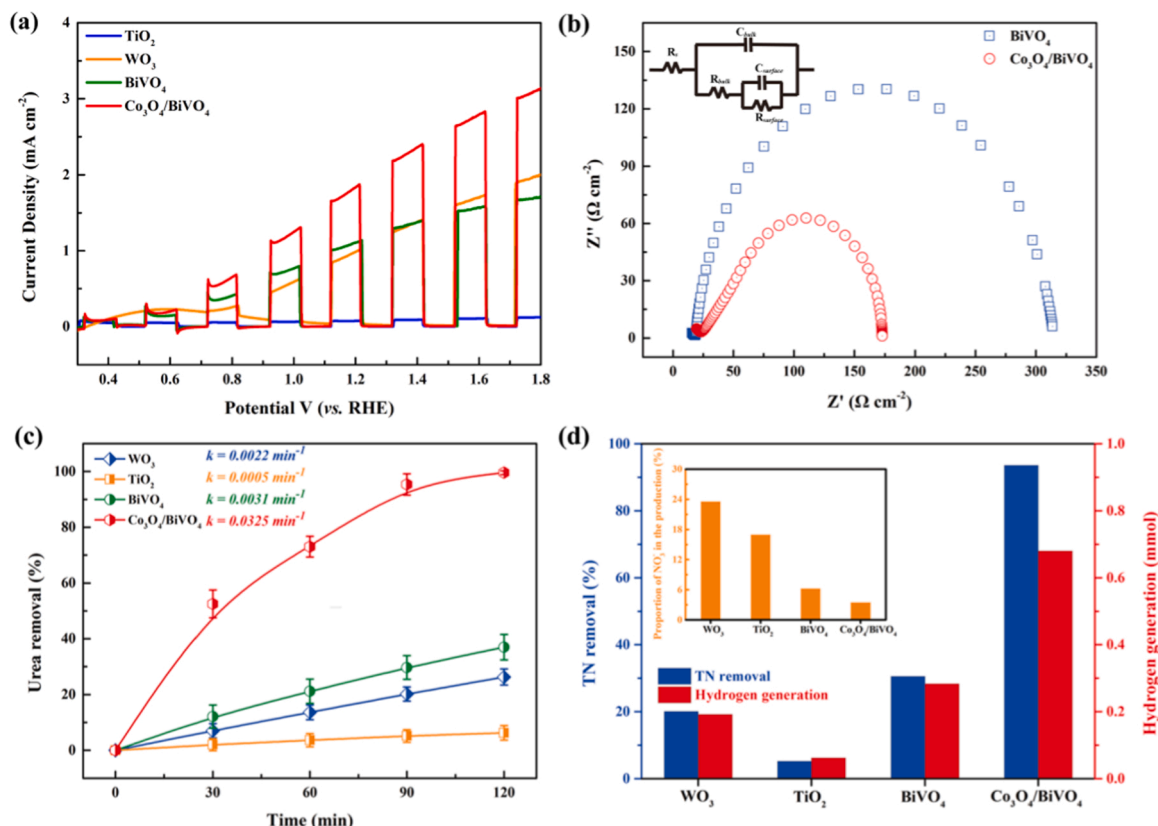


Fig. 4. (a) J - V curves of different electrodes (electrolyte: 0.5 M NaCl, scan rate: 10 mV s⁻¹); (b) electrochemical impedance spectroscopy (EIS) analysis of BiVO₄ and Co₃O₄/BiVO₄; (c) urea removal versus time by different electrodes; (d) TN removal, hydrogen generation and the proportion of nitrate in the product by different electrodes.

production was well shown in Fig. 4c-d. Meanwhile, Fig. 4c displayed the urea removal via WO₃, TiO₂, BiVO₄ and Co₃O₄/BiVO₄, of which the removal rate was obeyed the first-order kinetics. Obviously, urea removal in 120 min via Co₃O₄/BiVO₄ (99.5%) was much better than WO₃ (26.3%), TiO₂ (6.3%) and BiVO₄ (37.0%), in which the rate constant of Co₃O₄/BiVO₄ (0.0325 min⁻¹) was 14.8 times, 65.0 times and 10.5 times higher than that of WO₃ (0.0022 min⁻¹), TiO₂ (0.0005 min⁻¹) and BiVO₄ (0.0031 min⁻¹), respectively. Besides, Fig. 4d showed the TN removal and H₂ generation by WO₃, TiO₂, BiVO₄ and Co₃O₄/BiVO₄ via the photoelectrocatalytic treatment. Similarly, Co₃O₄/BiVO₄ photoanode showed the best performance on TN removal and H₂ production, in which 93.6% of TN was removed and 0.68 mmol H₂ was generated on the MoNiCuO_x/Cu cathode correspondingly. Meanwhile, TN removal via Co₃O₄/BiVO₄ was 3.1 times, 4.8 times and 17.9 times higher than BiVO₄, WO₃ and TiO₂, respectively; Correspondingly, H₂ generation via Co₃O₄/BiVO₄ was 2.4 times, 3.5 times and 11.0 times higher than BiVO₄, WO₃ and TiO₂, respectively. Markedly, the by-product (NO₃) was significantly suppressed, which was only 3.5% of urea was peroxidation. That was because the formed p-n heterojunction suppresses holes and electrons, which not only strengthened the ability of the photoanode to activate Cl⁻ oxidizing urea, but also facilitated the transfer of electrons in the conduction band (CB) to the MoNiCuO_x/Cu cathode for H₂ production [48,49]. Therefore, the performance on WO₃, TiO₂ and BiVO₄ of TN removal and hydrogen production were all lower than that of Co₃O₄/BiVO₄ photoanode. Hence, Co₃O₄/BiVO₄ photoanode showed the better performance.

3.4. Reaction mechanism

The Tauc plot and UPS spectra were applied to verify the band gap and valence band regions of BiVO₄ and Co₃O₄. The detailed results were

appended in Fig. S11, which take the band gap of 2.48 eV into account, the V_{BM} and C_{BM} of BiVO₄ were 2.53 and 0.05 V vs. RHE. Likewise, 1.43 (V_{BM}) and -0.38 (C_{BM}) V vs. RHE for Co₃O₄ (Table S3). Generally, the feasibility of urea removal and hydrogen generation were well demonstrated in Fig. 5 [24,50–52]. Firstly, because of the strong light responsiveness of p-n heterojunction, h^+ and electrons were easily produced on Co₃O₄/BiVO₄ photoanode under illumination (Eq. 3). Meanwhile, the electrons in the CB of Co₃O₄ flowed into the CB of BiVO₄, then transferred into the MoNiCuO_x/Cu cathode. Simultaneously, MoNiCuO_x/Cu cathode with large specific surface and multiple of MoNi₄ active sites can effectively adsorb H₂O in solution to form H⁺ (Eq. 4). Next, the other distributed MoO₂ active sites were able to bind H⁺ to form H₂ and desorb from the cathode surface (Eq. 5). On the other hand, h^+ were produced in both BiVO₄ and Co₃O₄, in which the h^+ of BiVO₄ flowed into the valence band (VB) of Co₃O₄. The generated h^+ available oxidized Cl⁻ to convert active chlorine (Cl[•] and Cl₂) (Eqs. 6–7). Thereafter, urea was oxidized to N₂ and CO₂ after a series of reactions by active chlorine (Eqs. 8–9). Furthermore, the concentration of different nitrogen-containing compounds are measured (Fig. S12), in which most of urea was constantly converted to N₂ and little part of urea was over-oxidized into NO₃. Critically, due to the thermodynamic decomposition of urea is much lower than water splitting (Eqs. 1–2), we compared the current density, in which the current density of decomposition of urea (4.2 mA cm⁻²) was much higher than water splitting (2.5 mA cm⁻²) (Fig. S13). Besides, the energy consumption and cost were calculated and the results were shown in Table S4. Meanwhile, the consumption and cost of urine treatment were 1.18 kWh m⁻³ and 0.094 \$ m⁻³ respectively, which were lower than splitting water (1.73 kWh m⁻³ and 0.138 \$ m⁻³) to produce the same amount of H₂. Notably, the proposed PEC system can not only treat the urine wastewater but also produce more H₂ with the lower cost. Finally, both denitrification and

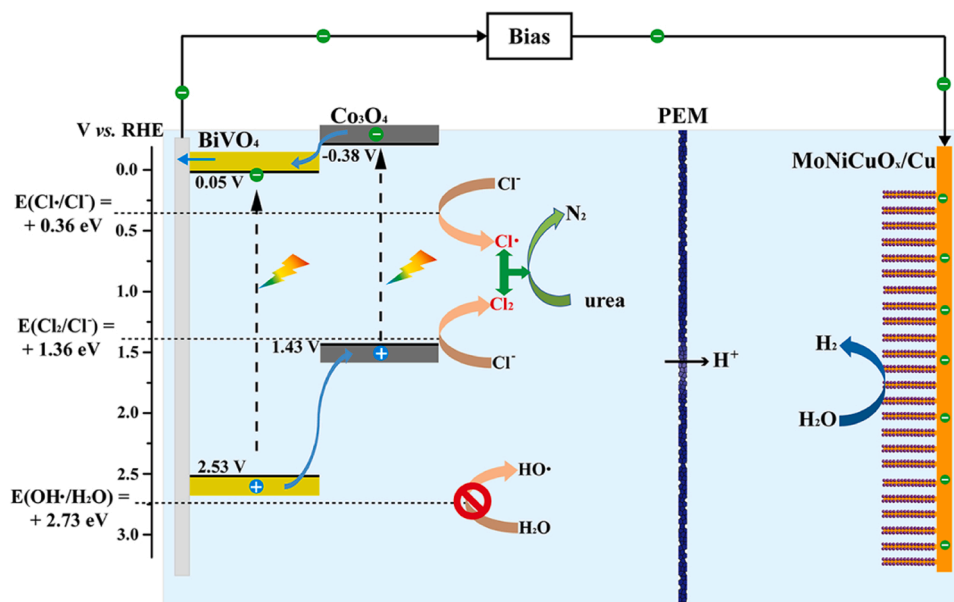
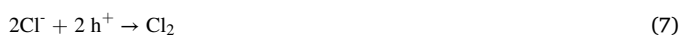


Fig. 5. Illustration of the TN removal and hydrogen generation mechanism in the photoelectrocatalytic system induced by $\text{Co}_3\text{O}_4/\text{BiVO}_4$ photoanode and $\text{MoNiCuO}_x/\text{Cu}$ cathode.

hydrogen energy recovery were realized. Besides, the concentration of active chlorine was detected during the reaction. As shown in Fig. S14a, the active chlorine concentration was constantly increased as the reaction progressed, in which $\text{Co}_3\text{O}_4/\text{BiVO}_4$ photoanode showed the best capacity of chlorine evolution reaction (CER) and generated 4.45 mg/L of active chlorine in 120 min. Moreover, the electron spin-resonance spectroscopy (ESR) analysis was applied to analyze the radical species in the reaction. Notably, the results of the ESR analysis were explained there were no $\text{HO}\cdot$ generated during the reaction. Furthermore, the oxidation of DMPO to DPMOX with active chlorine consisting of $\text{Cl}\cdot$ and Cl_2 (Fig. S14b) [52,53], which confirmed the urea removal process in Fig. 5. Additionally, benzoic acid (BA) was used probe the $\text{Cl}\cdot$, in which BA only reacted with $\text{Cl}\cdot$ [54] but did not react with Cl_2 . Besides, nitrobenzene (NB) only reacts with $\text{HO}\cdot$, which eliminated possible interference of $\text{HO}\cdot$. As shown in Fig. S14c, the removal of urea was dramatically decreased to 22.6% with the addition of BA while the removal of urea did not change obviously after adding NB, which further confirmed that $\text{Cl}\cdot$ was the main oxidant for urea degradation. Markedly, the concentrations of $\text{Cl}\cdot$ under different anode catalysis were detected and found the concentration of $\text{Cl}\cdot$ generated by $\text{Co}_3\text{O}_4/\text{BiVO}_4$ (1.38×10^{-7} M) was extremely strikingly higher than that of WO_3 (3.11×10^{-9} M), TiO_2 (1.01×10^{-11} M) and BiVO_4 (1.30×10^{-8} M) photoanodes (Fig. S14d), which confirmed the superior ability of $\text{Co}_3\text{O}_4/\text{BiVO}_4$ to generate $\text{Cl}\cdot$.



3.5. The effect of applied potential

The applied potential (vs. RHE) will significantly affect the performance of PEC system, in which the oxidative-capacity of the anode improved with the increase of applied potential. Hence, different applied potential was tested for PEC system research. In Fig. 6a, the removal rate of urea was increased with the increase of the applied potential. Meanwhile, 59.4%, 96.4%, 99.6% and 99.9% of urea were removed at 1.4 V, 1.6 V, 1.8 V and 2.0 V, respectively, which all obeyed the first-order kinetics. Similarly, the total organic carbon (TOC) removal and H_2 generated yield were also increased with the increase of the applied potential. However, the TN removal rate peaked at an applied potential of 1.8 V, in which 93.6% of TN was removed. With further research, it was found that urea would be per-oxidized to NO_3^- , and with the increase of the operating potential, the oxidative-capacity of the anode was continuously enhanced, resulting in more NO_3^- produced by urea peroxidation (Fig. S15a). Therefore, TN removal had instead declined when the applied potential was 2.0 V. Besides, considering about high applied potential requires more electric energy, the faradaic efficiency (FE) was used to determine the optimal applied potential. The applied potential of 1.8 V was the highest although all of the FE in different applied potentials were relatively low (Fig. S16). That is because the oxidation of urea is accomplished by $\text{Cl}\cdot$, in which $\text{Cl}\cdot$ was not completely reacted with urea and part remained in the solution, resulting in lower FE. If the concentration of urea is increased to enhance the reaction with $\text{Cl}\cdot$, the FE also increases simultaneously. To achieve the highest TN removal, the applied potential of 1.8 V was chosen for the PEC system.

3.6. The effect of initial Cl^- concentration

As mentioned, the urea removal was achieved by oxidative conversion of $\text{Cl}\cdot$. Thereafter, the effect of different initial concentrations of Cl^- were tested, which different concentration of Cl^- added into the simulated urine. As shown in Figs. 6c, 25.7% of urea was removed when no Cl^- were added, which may be the h^+ generated on the surface of $\text{Co}_3\text{O}_4/\text{BiVO}_4$ directly oxidized the urea. Obviously, the direct oxidation on the surface of catalyst resulted in very low removal efficiency (0.0024 min^{-1}). Conversely, with the introduction of Cl^- (25 mM), the removal efficiency was significantly improved, which reached

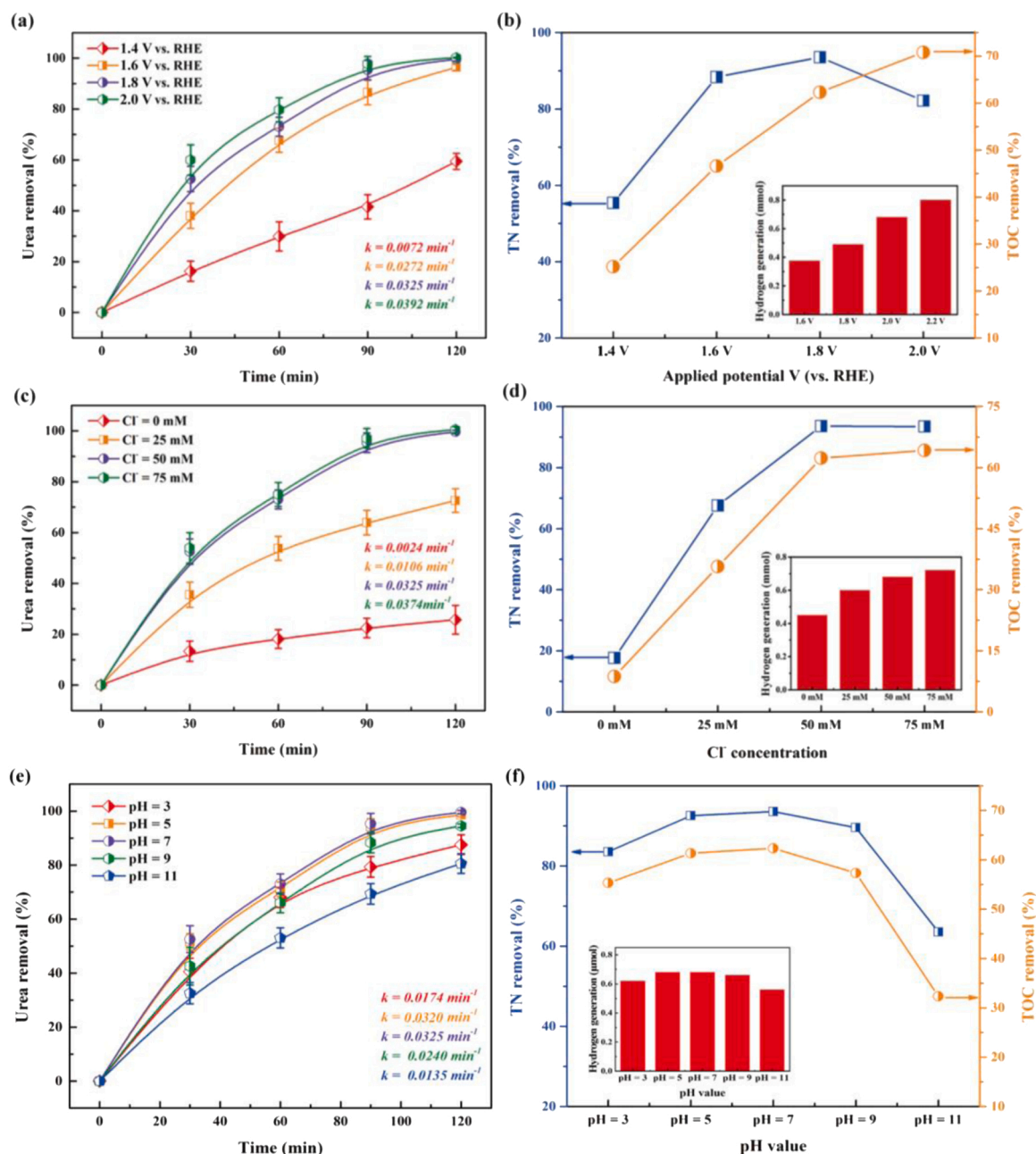


Fig. 6. Effect of applied potential on (a) urea removal and (b) TN removal, TOC removal and hydrogen generation; Effect of Cl^- concentration on (c) urea removal and (d) TN removal, TOC removal and hydrogen generation; Effect of pH value on (e) urea removal and (f) TN removal, TOC removal and hydrogen generation.

0.0106 min^{-1} . When the Cl^- concentration was further increased to 50 mM, the removal rate of urea was further improved (0.0325 min^{-1}). The ability of urea oxidation reached the peak due to the h^+ can activate Cl was limited. Certainly, the removal effect of urea showed no obvious improvement by increasing the Cl^- concentration (75 mM). Correspondingly, TOC removal, TN removal and H_2 generated yield were also continuously increased with the increase of the Cl^- concentration (Fig. 6d). Critically, the concentration of NO_3^- produced by peroxidation decreased with the increase of Cl^- concentration (Fig. S15b). Therefore, the suitable Cl^- concentration was 50 mM.

3.7. The effect of pH value

As described above, the thermodynamically favorable product of urea oxidation by $\text{Cl}\cdot$ is N_2 . However, pH value is the key factors for the generation of $\text{Cl}\cdot$. Therefore, the effects of pH value on the PEC

performance was investigated. In Fig. 6e and Fig. 6f, the good performance occurred under weakly acidic and neutral conditions (pH = 5 and 7), which showed the very similar yield of hydrogen generation and the removal of urea, TN and TOC. However, there was an obvious downward trend when the pH value keeps rising, of which the removal rate of urea was decreased to 0.0135 min^{-1} at pH = 11. Correspondingly, among TOC removal, TN removal and H_2 generated yield were also continuously dropped (Fig. 6f). $\text{Cl}\cdot$ was unstable existed under alkaline conditions, resulting in the dropping in oxidation of urea [54]. Additionally, 17.1% (5.14 ppm) of NO_3^- was generated when pH = 11, in which the selectivity of N_2 was extremely inhibited (Fig. S15c). On the other hand, as Co_3O_4 could be corroded under strong acid conditions [55], PEC performance, including the removal of urea, TN and TOC, as well as hydrogen production, will slightly decrease when pH = 3. Hence, the constructed PEC system showed superior performance under both weak acidic and neutral conditions.

3.8. Environmental implications

To further clarify the implications of the prepared PEC system, actual urine, as the targets, was employed to examine the practical application value. As shown in Fig. S17, TN of actual urine was removed 95.4% and 2.30 mmol of H₂ was produced simultaneously after 8 h, which maintained the high activity in a complex water matrix. Additionally, there were no obvious change in the micro-structure of the electrodes after urine-treatment (Fig. S18), and the removal of TN and H₂ generation were maintained at 92.3% and 0.59 mmol respectively after 5 consecutive runs (Fig. S19), which conformed the robust stability of the PEC system. More importantly, the produced hydrogen energy, as the environmentally friendly energy, is crucial for its practical industrial application. Overall, this PEC system can realize the urine transformation and hydrogen energy recovery, which meets the low-carbon requirements and realize the zero-carbon emission. Hence, the novel PEC technique has the great scientific and economic significance in environmental field.

4. Conclusion

This study proposed a novel dual-chamber PEC system, which constructed with Co₃O₄/BiVO₄ photoanode and MoNiCuO_x/Cu cathode to achieve effective TN removal and simultaneous recovery of hydrogen energy in urine treatment. Meanwhile, Co₃O₄/BiVO₄ photoanode converted Cl⁻ to Cl• with high selectivity for efficient TN removal, and MoNiCuO_x/Cu showed the much lower over-potential of HER (49 mV). Both TN removal and H₂ generation via PEC system were significantly improved. Additionally, PEC system showed good stability during cycling experiments, and also exhibited the similar performance for actual urine treatment. Critically, the cost of urea treatment was only 0.094 \$ m⁻³ and producing 0.68 mmol H₂. This study provides a new insight for the possible application of photoelectrocatalytic treatment for urine wastewater.

CRediT authorship contribution statement

Changhui Zhou: Conceptualization, Data curation, Writing – original draft, Writing – review & editing. **Jinhua Li:** Visualization, Investigation, Supervision. **Jiachen Wang:** Investigation, Data curation. **Yan Zhang:** Investigation, Data curation, Methodology. **Lei Li:** Methodology. **Tingsheng Zhou:** Methodology. **Chaoyue Xie:** Data curation. **Jing Bai:** Visualization, Supervision. **Hong Zhu:** Supervision. **Baoxue Zhou:** Conceptualization, Supervision, Project administration, Writing – review & editing.

Declaration of Competing Interest

The authors declare that they have no known competing financial interests or personal relationships that could have appeared to influence the work reported in this paper.

Data Availability

Data will be made available on request.

Acknowledgements

The authors would like to acknowledge the National Natural Science Foundation of China (No. 22178220 and 21875139) and the Center for Advanced Electronic Materials and Devices (AEMD) of Shanghai Jiao Tong University (SJTU) for support.

Appendix A. Supporting information

Supplementary data associated with this article can be found in the

online version at doi:10.1016/j.apcatb.2022.122229.

References

- [1] Z. Shen, Y. Zhang, C. Zhou, J. Bai, S. Chen, J. Li, J. Wang, X. Guan, M. Rahim, B. Zhou, Exhaustive denitrification via chlorine oxide radical reactions for urea based on a novel photoelectrochemical cell, *Water Res.* 170 (2020), 115357, <https://doi.org/10.1016/j.watres.2019.115357>.
- [2] A.N. Rollinson, J. Jones, V. Dupont, M.V. Twigg, Urea as a hydrogen carrier: a perspective on its potential for safe, sustainable and long-term energy supply, *Energy Environ. Sci.* 4 (4) (2011) 1216, <https://doi.org/10.1039/c0ee00705f>.
- [3] Z. Ma, H. Wang, H. Ma, S. Zhan, Q. Zhou, Three-dimensional crystalline-Ni₅P₄@amorphous-NiO_x core-shell nanosheets as bifunctional electrode for urea electro-oxidation and hydrogen evolution, *Fuel* 315 (2022), 123279, <https://doi.org/10.1016/j.fuel.2022.123279>.
- [4] W. Shi, J. Lian, Mesoporous Cu(OH)₂ nanowire arrays for urea electrooxidation in alkaline medium, *Mater. Chem. Phys.* 242 (2020), 122517, <https://doi.org/10.1016/j.matchemphys.2019.122517>.
- [5] K. Cho, M.R. Hoffmann, Urea degradation by electrochemically generated reactive chlorine species: products and reaction pathways, *Environ. Sci. Technol.* 48 (19) (2014) 11504–11511, <https://doi.org/10.1021/es5025405>.
- [6] B.K. Boggs, R.L. King, G.G. Botte, Urea electrolysis: direct hydrogen production from urine, *Chem. Commun.* 32 (2009) 4859–4861, <https://doi.org/10.1039/b905974a>.
- [7] R. Lan, S. Tao, J.T.S. Irvine, A direct urea fuel cell – power from fertiliser and waste, *Energy Environ. Sci.* 3 (4) (2010) 438–441, <https://doi.org/10.1039/b924786f>.
- [8] L. Deng, C.H. Huang, Y.L. Wang, Effects of combined UV and chlorine treatment on the formation of trichloronitromethane from amine precursors, *Environ. Sci. Technol.* 48 (5) (2014) 2697–2705, <https://doi.org/10.1021/es404116n>.
- [9] J. Ra, H. Yoom, H. Son, T.M. Hwang, Y. Lee, Transformation of an amine moiety of atenolol during water treatment with chlorine/UV: reaction kinetics, products, and mechanisms, *Environ. Sci. Technol.* 53 (13) (2019) 7653–7662, <https://doi.org/10.1021/acs.est.9b01412>.
- [10] F. Fang, Y. Zhang, J. Bai, J. Li, X. Mei, C. Zhou, M. Zhou, B. Zhou, Efficient urine removal, simultaneous elimination of emerging contaminants, and control of toxic chlorate in a photoelectrocatalytic-chlorine system, *Environ. Pollut.* 267 (2020), 115605, <https://doi.org/10.1016/j.envpol.2020.115605>.
- [11] Z. Shen, J. Bai, Y. Zhang, J. Li, T. Zhou, J. Wang, Q. Xu, B. Zhou, Efficient purification and chemical energy recovery from urine by using a denitrifying fuel cell, *Water Res.* 152 (2019) 117–125, <https://doi.org/10.1016/j.watres.2018.12.066>.
- [12] Y. Zhang, Y. Ji, J. Li, J. Bai, S. Chen, L. Li, J. Wang, T. Zhou, P. Jiang, X. Guan, B. Zhou, Efficient ammonia removal and toxic chlorate control by using BiVO₄/WO₃ heterojunction photoanode in a self-driven PEC-chlorine system, *J. Hazard. Mater.* 402 (2021), 123725, <https://doi.org/10.1016/j.jhazmat.2020.123725>.
- [13] Z. Zheng, Y.H. Ng, Y. Tang, Y. Li, W. Chen, J. Wang, X. Li, L. Li, Visible-light-driven photoelectrocatalytic activation of chloride by nanoporous MoS₂@BiVO₄ photoanode for enhanced degradation of bisphenol A, *Chemosphere* 263 (2021), 128279, <https://doi.org/10.1016/j.chemosphere.2020.128279>.
- [14] X. Li, M. Kan, T. Wang, Z. Qin, T. Zhang, X. Qian, Y. Kuwahara, K. Mori, H. Yamashita, Y. Zhao, The ClO₂-generation and chlorate suppression in photoelectrochemical reactive chlorine species systems on BiVO₄ photoanodes, *Appl. Catal. B: Environ.* 296 (2021), <https://doi.org/10.1016/j.apcatb.2021.120387>.
- [15] T. Zhou, L. Li, J. Li, J. Wang, J. Bai, L. Xia, Q. Xu, B. Zhou, Electrochemically reduced TiO₂ photoanode coupled with oxygen vacancy-rich carbon quantum dots for synergistically improving photoelectrochemical performance, *Chem. Eng. J.* 425 (2021), 131770, <https://doi.org/10.1016/j.cej.2021.131770>.
- [16] T. Zhou, S. Chen, L. Li, J. Wang, Y. Zhang, J. Li, J. Bai, L. Xia, Q. Xu, M. Rahim, B. Zhou, Carbon quantum dots modified anatase/rutile TiO₂ photoanode with dramatically enhanced photoelectrochemical performance, *Appl. Catal. B Environ.* 269 (2020), 118776, <https://doi.org/10.1016/j.apcatb.2020.118776>.
- [17] J. Bai, B. Zhang, J. Li, B. Zhou, Photoelectrocatalytic generation of H₂ and S from toxic H₂S by using a novel BiOI/WO₃ nanoflake array photoanode, *Front. Energy* 15 (3) (2021) 744–751, <https://doi.org/10.1007/s11708-021-0775-7>.
- [18] Z. Chi, J. Zhao, Y. Zhang, H. Yu, H. Yu, Coral-like WO₃/BiVO₄ photoanode constructed via morphology and facet engineering for antibiotic wastewater detoxification and hydrogen recovery, *Chem. Eng. J.* 428 (2022), 131817, <https://doi.org/10.1016/j.cej.2021.131817>.
- [19] Y.-f. Su, G.-B. Wang, D.T.F. Kuo, M.-I. Chang, Y.-h. Shih, Photoelectrocatalytic degradation of the antibiotic sulfamethoxazole using TiO₂/Ti photoanode, *Appl. Catal. B Environ.* 186 (2016) 184–192, <https://doi.org/10.1016/j.apcatb.2016.01.003>.
- [20] J. Zhou, X. An, Q. Tang, H. Lan, Q. Chen, H. Liu, J. Qu, Dual channel construction of WO₃ photocatalysts by solution plasma for the persulfate-enhanced photodegradation of bisphenol A, *Appl. Catal. B Environ.* 277 (2020), 119221, <https://doi.org/10.1016/j.apcatb.2020.119221>.
- [21] X. Cheng, Q. Cheng, X. Deng, P. Wang, H. Liu, A facile and novel strategy to synthesize reduced TiO₂ nanotubes photoelectrode for photoelectrocatalytic degradation of diclofenac, *Chemosphere* 144 (2016) 888–894, <https://doi.org/10.1016/j.chemosphere.2015.09.070>.
- [22] D. Wang, Y. He, N. Zhong, Z. He, Y. Shen, T. Zeng, X. Lu, J. Ma, S. Song, In situ chloride-mediated synthesis of TiO₂ thin film photoanode with enhanced photoelectrochemical activity for carbamazepine oxidation coupled with

- simultaneous cathodic H₂ production and CO₂ conversion to fuels, *J. Hazard. Mater.* 410 (2021), 124563, <https://doi.org/10.1016/j.jhazmat.2020.124563>.
- [23] C. Zhou, J. Li, Y. Zhang, J. Bai, L. Li, X. Mei, X. Guan, B. Zhou, Novel denitrification fuel cell for energy recovery of nitrate-N and TN removal based on NH₄⁺ generation on a CNW@CF cathode, *Environ. Sci. Technol.* 56 (4) (2022) 2562–2571, <https://doi.org/10.1021/acs.est.1c04363>.
- [24] K.H. Ye, H. Li, D. Huang, S. Xiao, W. Qiu, M. Li, Y. Hu, W. Mai, H. Ji, S. Yang, Enhancing photoelectrochemical water splitting by combining work function tuning and heterojunction engineering, *Nat. Commun.* 10 (1) (2019) 3687, <https://doi.org/10.1038/s41467-019-11586-y>.
- [25] J. Feng, J. Bian, L. Bai, S. Xi, Y. Wang, C. Chen, L. Jing, Efficient wide-spectrum photocatalytic overall water splitting over ultrathin molecular nickel phthalocyanine/BiVO₄ Z-scheme heterojunctions without noble metals, *Appl. Catal. B Environ.* 295 (2021), 120260, <https://doi.org/10.1016/j.apcatb.2021.120260>.
- [26] J. Wang, T. Zhou, Y. Zhang, L. Li, C. Zhou, J. Bai, J. Li, H. Zhu, B. Zhou, Type-II heterojunction CdIn₂S₄/BiVO₄ coupling with QDs to improve PEC water splitting performance synergistically, *ACS Appl. Mater. Interfaces* 14 (40) (2022) 45392–45402, <https://doi.org/10.1021/acsami.2c12618>.
- [27] H. Bai, X. Li, Y. Zhao, W. Fan, Y. Liu, Y. Gao, D. Xu, J. Ding, W. Shi, Fabrication of BiVO₄-Ni/Co₃O₄ photoanode for enhanced photoelectrochemical water splitting, *Appl. Surf. Sci.* 538 (2021), 148150, <https://doi.org/10.1016/j.apsusc.2020.148150>.
- [28] Y. Wang, D. Yu, W. Wang, P. Gao, S. Zhong, L. Zhang, Q. Zhao, B. Liu, Synthesizing Co₃O₄-BiVO₄/g-C₃N₄ heterojunction composites for superior photocatalytic redox activity, *Sep. Purif. Technol.* 239 (2020), 116562, <https://doi.org/10.1016/j.seppur.2020.116562>.
- [29] M. Long, W. Cai, J. Cai, B. Zhou, X. Chai, Y. Wu, Efficient photocatalytic degradation of phenol over Co₃O₄/BiVO₄ composite under visible light irradiation, *J. Phys. Chem. B* 110 (2011) 20211–20216.
- [30] P. Hu, M. Long, Cobalt-catalyzed sulfate radical-based advanced oxidation: a review on heterogeneous catalysts and applications, *Appl. Catal. B Environ.* 181 (2016) 103–117, <https://doi.org/10.1016/j.apcatb.2015.07.024>.
- [31] Z. Dong, F. Lin, Y. Yao, L. Jiao, Crystalline Ni(OH)₂/amorphous NiMoOx mixed-catalyst with Pt-Like performance for hydrogen production, *Adv. Energy Mater.* 9 (46) (2019) 1902703, <https://doi.org/10.1002/aenm.201902703>.
- [32] J.K. Nørskov, J. Rossmeisl, A. Logadottir, L. Lindqvist, Origin of the overpotential for oxygen reduction at a fuel-cell cathode, *J. Phys. Chem. B* 108 (2004) 17886–17892.
- [33] X. Zou, Y. Zhang, Noble metal-free hydrogen evolution catalysts for water splitting, *Chem. Soc. Rev.* 44 (15) (2015) 5148–5180, <https://doi.org/10.1039/c4cs00448e>.
- [34] Y. Zhang, B. Ouyang, J. Xu, S. Chen, R.S. Rawat, H.J. Fan, 3D porous hierarchical nickel-molybdenum nitrides synthesized by RF plasma as highly active and stable hydrogen-evolution-reaction electrocatalysts, *Adv. Energy Mater.* 6 (11) (2016) 1600221, <https://doi.org/10.1002/aenm.201600221>.
- [35] F. Wang, Y. Sun, Y. He, L. Liu, J. Xu, X. Zhao, G. Yin, L. Zhang, S. Li, Q. Mao, Y. Huang, T. Zhang, B. Liu, Highly efficient and durable MoNiNC catalyst for hydrogen evolution reaction, *Nano Energy* 37 (2017) 1–6, <https://doi.org/10.1016/j.nanoen.2017.04.050>.
- [36] L. Yu, I.K. Mishra, Y. Xie, H. Zhou, J. Sun, J. Zhou, Y. Ni, D. Luo, F. Yu, Y. Yu, S. Chen, Z. Ren, Ternary Ni₂(1-x)Mo_{2x}P nanowire arrays toward efficient and stable hydrogen evolution electrocatalysis under large-current-density, *Nano Energy* 53 (2018) 492–500, <https://doi.org/10.1016/j.nanoen.2018.08.025>.
- [37] A. Sahasrabudhe, H. Dixit, R. Majee, S. Bhattacharyya, Value added transformation of ubiquitous substrates into highly efficient and flexible electrodes for water splitting, *Nat. Commun.* 9 (1) (2018) 2014, <https://doi.org/10.1038/s41467-018-04358-7>.
- [38] J. Tian, Q. Liu, N. Cheng, A.M. Asiri, X. Sun, Self-supported Cu₃P nanowire arrays as an integrated high-performance three-dimensional cathode for generating hydrogen from water, *Angew. Chem. Int. Ed. Engl.* 53 (36) (2014) 9577–9581, <https://doi.org/10.1002/anie.201403842>.
- [39] C. Song, Z. Zhao, X. Sun, Y. Zhou, Y. Wang, D. Wang, In situ growth of Ag nanodots decorated Cu₂O porous nanobelts networks on copper foam for efficient HER electrocatalysis, *Small* 15 (29) (2019) 1804268, <https://doi.org/10.1002/smll.201804268>.
- [40] W. He, J. Zhang, S. Dieckhofer, S. Varhade, A.C. Brix, A. Lielpetere, S. Seisel, J.R. C. Junqueira, W. Schuhmann, Splicing the active phases of copper/cobalt-based catalysts achieves high-rate tandem electroreduction of nitrate to ammonia, *Nat. Commun.* 13 (1) (2022) 1129, <https://doi.org/10.1038/s41467-022-28728-4>.
- [41] P. Wang, J. Li, Y. Xu, C. Zhou, Y. Zhang, L. Zha, B. Zhang, J. Bai, B. Zhou, Efficient hydrogen generation and total nitrogen removal for urine treatment in a neutral solution based on a self-driving nano photoelectrocatalytic system, *Nanomaterials* 11 (11) (2021), <https://doi.org/10.3390/nano11112777>.
- [42] C. Zhou, J. Bai, Y. Zhang, J. Li, Z. Li, P. Jiang, F. Fang, M. Zhou, X. Mei, B. Zhou, Novel 3D Pd-Cu(OH)₂/CF cathode for rapid reduction of nitrate-N and simultaneous total nitrogen removal from wastewater, *J. Hazard. Mater.* 401 (2020), 123232, <https://doi.org/10.1016/j.jhazmat.2020.123232>.
- [43] S. Qin, Y. Duan, X.L. Zhang, L.R. Zheng, F.Y. Gao, P.P. Yang, Z.Z. Niu, R. Liu, Y. Yang, X.S. Zheng, J.F. Zhu, M.R. Gao, Ternary nickel-tungsten-copper alloy rivals platinum for catalyzing alkaline hydrogen oxidation, *Nat. Commun.* 12 (1) (2021) 2686, <https://doi.org/10.1038/s41467-021-22996-2>.
- [44] J. Zhang, T. Wang, P. Liu, Z. Liao, S. Liu, X. Zhuang, M. Chen, E. Zschech, X. Feng, Efficient hydrogen production on MoNi₄ electrocatalysts with fast water dissociation kinetics, *Nat. Commun.* 8 (2017) 15437, <https://doi.org/10.1038/ncomms15437>.
- [45] Z. Ge, B. Fu, X. Li, J. Zhao, B. Ma, Z. Luo, Y. Chen, Heterostructure of Mn₃O₄ nanoparticles on Cu(OH)₂ nanowire arrays for electrocatalytic water oxidation, *J. Power Sources* 476 (2020), 228731, <https://doi.org/10.1016/j.jpowsour.2020.228731>.
- [46] Y. Wu, L. Xu, W. Xin, T. Zhang, J. Cao, B. Liu, Q. Qiang, Z. Zhou, T. Han, S. Cao, W. Xiao, J. Wei, Rational construction of 3D MoNi/NiMoOx@NiFe LDH with rapid electron transfer for efficient overall water splitting, *Electrochim. Acta* 369 (2021), 137680, <https://doi.org/10.1016/j.electacta.2020.137680>.
- [47] Y. Zhang, W. Tang, J. Bai, J. Li, J. Wang, T. Zhou, X. Guan, B. Zhou, Highly efficient removal of total nitrogen and dissolved organic compound in waste reverse osmosis concentrate mediated by chlorine radical on 3D Co₃O₄ nanowires anode, *J. Hazard. Mater.* 424 (2022), 127662, <https://doi.org/10.1016/j.jhazmat.2021.127662>.
- [48] Y. Guo, Y. Dai, W. Zhao, H. Li, B. Xu, C. Sun, Highly efficient photocatalytic degradation of naphthalene by Co₃O₄/Bi₂O₃/CO₂ under visible light: A novel p-n heterojunction nanocomposite with nanocrystals/lotus-leaf-like nanosheets structure, *Appl. Catal. B Environ.* 237 (2018) 273–287, <https://doi.org/10.1016/j.apcatb.2018.05.089>.
- [49] W. He, L. Liu, T. Ma, H. Han, J. Zhu, Y. Liu, Z. Fang, Z. Yang, K. Guo, Controllable morphology CoFe₂O₄/g-C₃N₄ p-n heterojunction photocatalysts with built-in electric field enhance photocatalytic performance, *Appl. Catal. B Environ.* 306 (2022), 121107, <https://doi.org/10.1016/j.apcatb.2022.121107>.
- [50] H.G. Cha, K.S. Choi, Combined biomass valorization and hydrogen production in a photoelectrochemical cell, *Nat. Chem.* 7 (4) (2015) 328–333, <https://doi.org/10.1038/nchem.2194>.
- [51] T.W. Kim, K.-S. Choi, Nanoporous BiVO₄ photoanodes with dual-layer oxygen evolution catalysts for solar water splitting, *Science* 343 (6147) (2014) 990–994, <https://doi.org/10.1126/science.1246913>.
- [52] Z. Yan, Z. Dai, W. Zheng, Z. Lei, J. Qiu, W. Kuang, W. Huang, C. Feng, Facile ammonium oxidation to nitrogen gas in acid wastewater by in situ photogenerated chlorine radicals, *Water Res.* 205 (2021), 117678, <https://doi.org/10.1016/j.watres.2021.117678>.
- [53] T. Li, Y. Jiang, X. An, H. Liu, C. Hu, J. Qu, Transformation of humic acid and halogenated byproduct formation in UV-chlorine processes, *Water Res.* 102 (2016) 421–427, <https://doi.org/10.1016/j.watres.2016.06.051>.
- [54] J. Fang, Y. Fu, C. Shang, The roles of reactive species in micropollutant degradation in the UV/free chlorine system, *Environ. Sci. Technol.* 48 (3) (2014) 1859–1868, <https://doi.org/10.1021/es4036094>.
- [55] Y. Zhang, X. Huang, J. Li, J. Bai, C. Zhou, L. Li, J. Wang, M. Long, X. Zhu, B. Zhou, Rapid conversion of Co²⁺ to Co³⁺ by introducing oxygen vacancies in Co₃O₄ nanowire anodes for nitrogen removal with highly efficient H₂ recovery in urine treatment, *Environ. Sci. Technol.* 56 (13) (2022) 9693–9701, <https://doi.org/10.1021/acs.est.2c00729>.